EXAFS and XANES Investigation of the ETS-10 Microporous Titanosilicate

C. Prestipino,*,† P. L. Solari,‡ and C. Lamberti†

Department of Inorganic, Physical and Materials Chemistry and NIS Centre of Excellence, Via P. Giuria 7, I-10125 Torino, Italy, and ESRF, rue J. Horowitz 6, BP 220 F-38043 Grenoble France

In this work, we report state-of-the-art analysis of both Ti K-edge high-resolution XANES and EXAFS data collected on the ETS-10 molecular sieve at the GILDA BM8 beamline of the ESRF facility. The interatomic distances and the angles obtained in our EXAFS study are in fair agreement with the single-crystal XRD data of Wang and Jacobson (*Chem. Commun.* **1999,** 973) and with the recent ab initio periodic study of Damin et al. (*J. Phys. Chem. B* **2004,** *108,* 1328) Differently from previous EXAFS work (*J. Phys. Chem.* **1996,** *100,* 449), our study supports a model of ETS-10 where the Ti atoms are bonded with two equivalent axial oxygen atoms. This model is also able to reproduce the edge and the post-edge region of the XANES spectrum. Conversely, the weak but well-defined pre-edge peak at 4971.3 eV can be explained only by assuming that a fraction of Ti atoms are in a local geometry similar to that of the pentacoordinated Ti sites in the ETS-4 structure. These Ti atoms in ETS-10 should be the terminal of the $-Ti-O-Ti-O-Ti-$ chains, of which the actual number is strongly increased by the high crystal defectivity (Ti vacancies).

1. Introduction

Microporous titanosilicates have been of interest since the discovery of important catalytic properties in titanium silicalite-1 (TS-1)[1] in oxidation and epoxidation reactions.[2–5] Among the huge number of porous titanosilicates, ETS-10, first reported by Kuznicki et al.,[6] occupies an important role owing to its interesting chemical and physical properties. Because of the high number of counterions present in the material, this molecular sieve has been appreciated for its ionic exchange properties[6,7] and as a bare catalyst.[8]

The much higher density of framework Ti(IV) centers with respect to other titanosilicates, such as TS-1[2–5] or Ti-β,[9] makes ETS-10 a promising photocatalyst. Its advantage, with respect to the classical high-surface-area TiO_2 oxide, consists of a three-dimensional microporous structure that provides to ETS-10 a shape selectivity toward the photodegradation of large organic molecules.[10,11] Very recently, Llabrés i Xamena et al.[12] have enhanced the activity in the shape-selectivity photocatalytic degradation of large aromatic molecules of ETS-10 by controlled defects production with fluoridic acid.

1.1. Brief Overview of the Structure of ETS-10. ETS-10 is a microporous titanosilicate with as-synthesized stoichiometry of $(Na, K)_2TiSi_5O_{13}$. For the first time, a convincing model of the structure of the ETS-10 framework was proposed by Anderson et al.[13] on the basis of a detailed high-resolution electron microscopy (HREM), NMR, powder x-ray diffraction (XRD), and structural modeling study. The same authors successively reported a deeper discussion on the model elsewhere.[14,15] However, up to 1999, the small-crystal size of samples of ETS-10 has prevented accurate structure refinement from single-crystal data, despite efforts to improve the syntheses. After that time, Wang and Jacobson[16] have been able to grow crystals with the necessary size to perform an accurate single-crystal analysis. A much more accurate knowledge of the structure of this material has consequently been achieved.

Its structure is formed by chains of corner-sharing TiO_6 octahedra linked to each other by tetrahedral SiO_4 units, generating a large-pore (twelve-membered ring) and forming a three-dimensional channel structure. Although the material is crystalline, it is characterized by a high level of disorder, owing to the possibility to build the crystal with different stacking arrangements. In fact, although two "ideal" polymorphs of ETS-10 have been identified, each formed by a particular stacking arrangement of the (001) layer, in reality, the stacking sequence is virtually random, resulting in an inherently disordered structure. The two polymorphs are shown in Figure 1. Polymorph A (tetragonal, $P4_1$ or $P4_3$) is formed by a zigzag stacking of layers, while polymorph B (monoclinic, $C2/c$) results from a diagonal stacking arrangement. The occurrence of stacking defects has even been revealed by the electron microscopy studies by Anderson et al.[13–15,17] This structural complexity has prevented the use of standard approaches for the refinement of the diffraction data, complicating the structure solving process.

One of the most interesting aspects of the ETS-10 structure is its possibility to be thought of as a network of one-dimensional TiO_2 semiconductor "quantum wires" embedded in a siliceous insulating matrix. This idea was first introduced by Torino's group,[18,19] who by following this concept have been able to explain the main features of the UV–vis spectrum of this material. A serious understanding of the electronic properties of ETS-10 came only later in the ab initio works of Bordiga et al.[20] and of Damin et al.[21]

1.2. Previous XAFS Study of ETS-10. Extended x-ray absorption fine structure (EXAFS) spectroscopy is an important tool for the characterization of new materials, particularly when a degree of disorder is present in the structure. The first application of this techniques on ETS-10 is the work of Davis et al.,[22] which appeared in 1995, just one year after the structure proposed by Anderson et al.[13] Successively, a more accurate

---

* Corresponding author: C. Prestipino, phone +39011-6707841; fax +39011-6707855; e-mail carmelo.prestipino@unito.it.
† Department of Inorganic, Physical and Materials Chemistry and NIS Centre of Excellence.
‡ ESRF.

XAS Study of ETS-10 Titanosilicate

J. Phys. Chem. B, Vol. 109, No. 27, 2005 **13133**
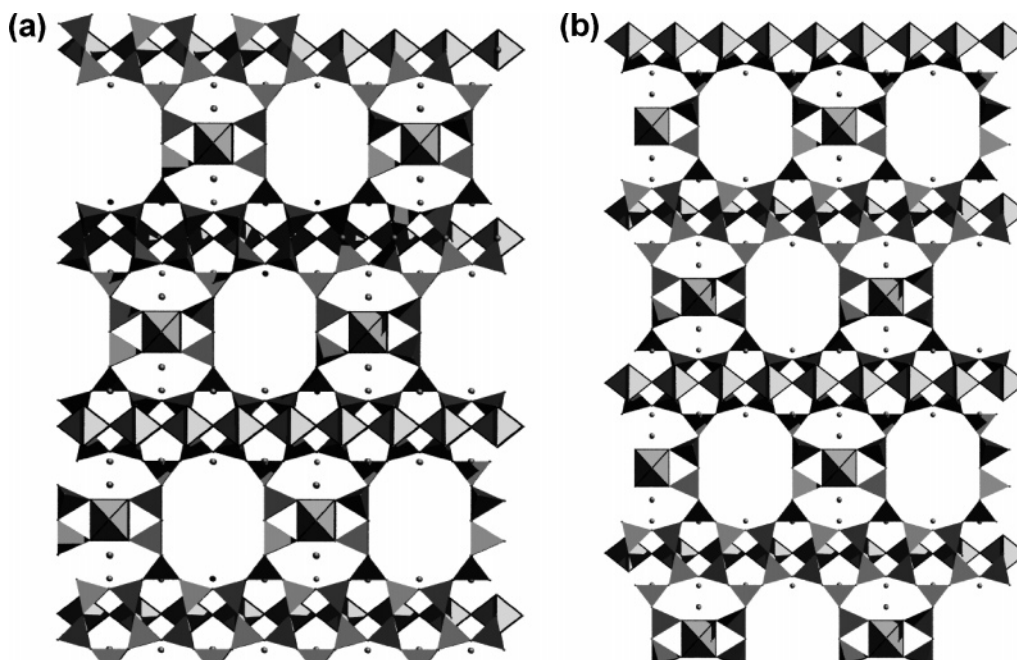
Figure 1. Structure of the two ideal polymorphs of ETS-10. Part (a), polymorph A; part (b), polymorph B. Octahedra and tetrahedra represent [TiO$_6$] and [SiO$_4$] units, respectively. Extraframework white spheres represent Na$^+$ cations.

data analysis, based on the multiple scattering approach, has been reported by Sankar et al.[23] EXAFS spectroscopy has also been used to study the local environment of Er^{3+} and Co^{2+} counterions hosted in the ETS-10 channels.[24,25] Also, the degree of defectivity of the framework has been subjected to EXAFS investigations.[12,26]

Among all these works, the one of Sankar et al.[23] is the most famous, because it is the only one able to present a local model for the Ti environment able to reproduce the whole EXAFS signal (i.e., up to the second Ti and Si shells), in which contributions appear up to about 3.6 Å in R space. This model is based on the presence of four equivalent Ti−O−Si contributions, perpendicular to the −Ti−O−Ti−O− chain (characterized by a unique Ti−O distance of 2.02 Å), and two unequivalent Ti−O contributions along the chain, characterized by significantly different first-shell Ti−O distances of 1.71 and 2.11 Å.[23]

The presence of short and long Ti−O distances along the −Ti−O−Ti−O− chain is not apparent either in the model proposed by Wang and Jacobson[16] on the basis of single-crystal diffraction or in the computational results of Sankar himself, based on a periodic atomistic approach,[23] or in those of Damin et al.,[21] based on a periodic ab initio method. In all cases, two equivalent axial Ti−O distances are found at 1.872 Å (by Wang and Jacobson[16]), at 1.88 Å (by Damin et al.[21]), and at 1.90 Å (atomistic approach by Sankar et al.[23]).

Regarding the angles of the −Ti−O−Ti−O− chain, an almost linear situation emerges from both the Wang and Jacobson model[16] (O−Ti−O = 180.0°; Ti−O−Ti = 177.9°) and the Damin model[21] (O−Ti−O = 180.0°; Ti−O−Ti = 179.2°). Conversely, the presence of a short and long Ti−O distance along the −Ti−O−Ti−O− chain causes a Ti−O−Ti angle of 165°, as optimized in the EXAFS analysis by Sankar et al.[23]

The aim of the present work is to rationalize the literature results using new x-ray absorption near-edge structure (XANES) and EXAFS data, collected on a third-generation synchrotron radiation facility, which have been analyzed using FEFF8.2[27] and GNXAS[28,29] codes, respectively.

2. Experimental and Methods

A Na-enriched ETS-10 has been obtained from a commercial (Na, K)-ETS-10 sample, kindly supplied by Engelhard (Iselin, NJ), according to standard exchanged procedures as described elsewhere.[30] Its external surface area is 21 m^2 g^{-1} (*t*-plot volumetric measurements with N$_2$ made with a Micromeritics ASAP 2010 instrument).

High-resolution (better than 0.3 eV at 5 keV) XANES spectra have been collected in transmission mode at liquid nitrogen temperature, with a sampling step of 0.1 eV across the edge, at the GILDA BM8 beamline of the ESRF storage ring using a flat Si(111) double-crystal monochromator. Harmonic rejection has been obtained by using a pair of flat, Pt-coated mirrors working at 10 mrad (critical energy E_c = 8300 eV). To calibrate the energy scale, a Ti metal foil has been located after the sample, and its reference spectrum has been acquired simultaneously with those of the sample, according to the geometry described elsewhere.[31] The maximum of the first pre-edge peak of Ti metal has been defined as 4964.2 eV. The EXAFS spectra, collected three times and averaged before the data analysis, have been sampled up to 5800 eV with a variable step in energy resulting in a maximum step of 0.05 Å^{-1} in k-space. A detailed description of the cell used to perform in situ XANES and EXAFS spectra has been reported elsewhere.[32]

The data analysis of the near-edge region has been performed using the FEFF 8.2 code,[27] in the frame of the full multiple scattering XANES simulation. The calculations have been performed using a spherical cluster with a radius of 7 Å, around the absorbing Ti atom, and the Hedin−Lundqvist exchange potential.

The extended region of the X-ray absorption spectrum has been analyzed using the GNXAS code,[28,29] which is able to take into account multiple scattering contributions. With respect to what is needed for the XANES simulation, owing to the significantly lower mean free path that the photoelectron has in the EXAFS region, a much smaller cluster is needed to simulate the EXAFS signal. The adopted cluster is reported in Figure 2, where Ti$_a$ represents the absorbing atom and where symmetrically unequivalent atoms are numbered to allow a
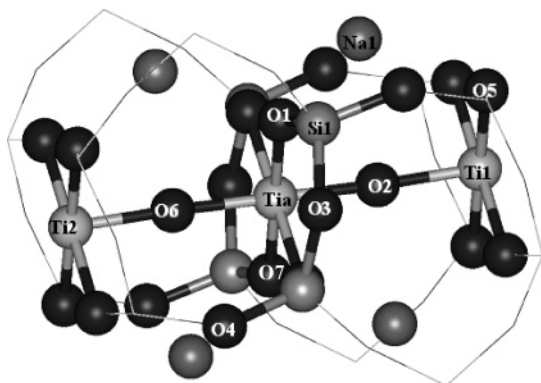
Figure 2. Cluster used to simulate the EXAFS spectrum. The Ti absorber atom is labeled as Tia. All the atoms reported here as full spheres have been included in the simulations. Different atoms of the same chemical species have been numbered to better define in the text the scattering paths included in the fitting procedure.

better path recognition in the discussion section. Note that O2 and O6 are equivalent first-shell atoms in the Wang–Damin model,[16,21] but they are not in the Sankar one.[23]

3. Results and Discussion

3.1. XANES. The experimental XANES spectrum of ETS-10 is reported in Figure 3a as full line. It is characterized by a well-defined pre-edge peak at 4971.3 eV of low intensity (0.22 in normalized μx) followed by two shoulders at 4974.4 and 4978.1 eV and by an intense white line at 4985.3 eV followed by a second resonance around 4996 eV, of comparable intensity. At higher energies, structured features are observed.

The result of the simulations of XANES spectra obtained using the Wang–Damin[16,21] and Sankar[23] models for constructing the FEFF8.2 input file are reported in Figure 3a as dashed and dotted lines, respectively. Perfect octahedra are expected to have no pre-edge features in the XANES spectrum, as both $A_{1g} \rightarrow T_{2g}$ and $A_{1g} \rightarrow E_g$ electronic transitions are Laporte forbidden. Anatase model compound, exhibiting just a small distortion of the $[TiO_6]$ units, results in a complex quadruplet of pre-edge features of very week intensity;[33,34] see the full line curve in Figure 3b. Consequently, the presence of the well-defined pre-edge peak at 4971.3 eV in the experimental XANES spectrum (full line in Figure 3a), clearly reflects the rupture of the octahedral symmetry around the Ti atoms resulting in the breakdown of the local inversion symmetry and thus in a mixing of 3d and 4p orbitals.[35,36] This fact seems to favor the Sankar model, as it foresees a much higher distortion of the $[TiO_6]$ unit. In fact, the XANES spectrum, simulated according to the Sankar model (dotted curve in Figure 3a), presents a well-defined pre-edge peak of comparable intensity with the experimental one (full curve), but the energy difference between its peak position and the edge is strongly underestimated.

On the other hand, the Wang–Damin model results in an XANES spectrum (dashed curve in Figure 3) with a structured feature in the pre-edge region typical of low distorted octahedra with chain structures.[33,34] No defined pre-edge peak is present in this simulation, owing to a much more regular $[TiO_6]$ unit foreseen in the Wang–Damin model. It is however worth noting that this model and the corresponding XANES simulation do not account for the defectivity of the −Ti−O−Ti−O−Ti− chains, which are often interrupted by a Ti vacancy.[6,15] Chain interruption will result in a strong distortion in the octahedral symmetry of the two $[TiO_6]$ units adjacent to the Ti vacancy, which become chain-terminal Ti sites. Terminal and regular Ti atoms must contribute to the overall experimental XANES
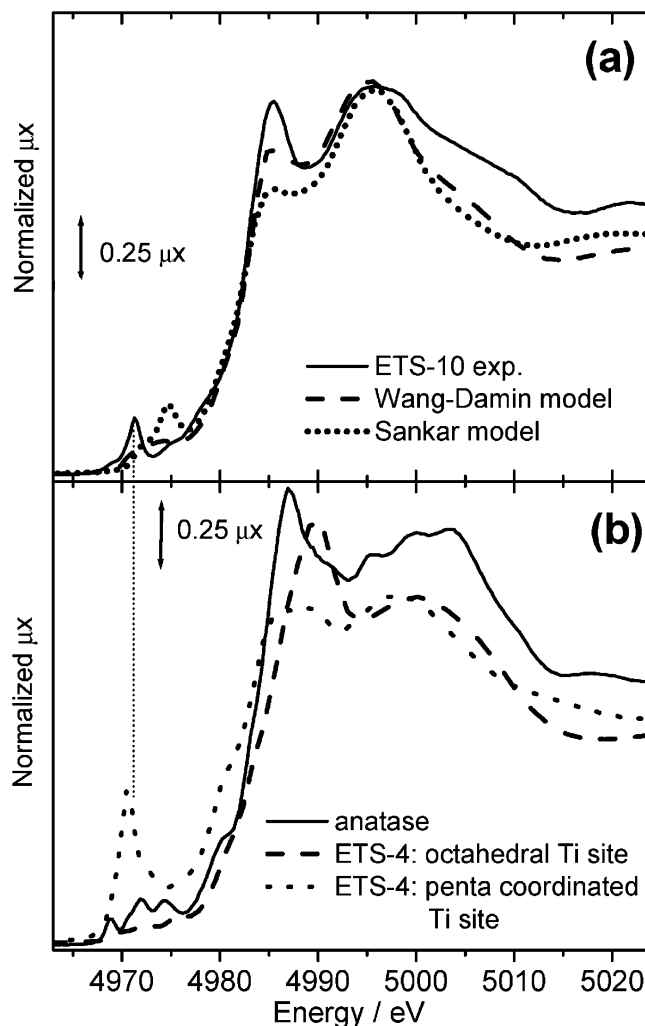
Figure 3. Part (a). Experimental (full line) and theoretical (dashed and dotted lines; see legend) XANES spectra of ETS-10. Part (b). Experimental XANES spectrum of anatase model compound (full line) together with the computed XANES spectra for the pentacoordinated and esa-coordinated (octahedral-like) Ti sites of the ETS-4 structure, dotted and dashed lines, respectively. The dotted vertical line evidences how the pre-edge feature observed in the experimental spectrum of ETS-10 (attributed to chain-terminal Ti atoms) appears very close to that obtained in the computation of the pentacoordinated Ti sites in ETS-4.

spectrum with completely different edge and pre-edge features. The more abundant regular Ti species are expected to be characterized by an XANES spectrum similar to that simulated according to the Wang–Damin model (dashed line in Figure 3a). The much less abundant terminal Ti species are probably the origin of the well-defined pre-edge peak at 4971.3 eV observed in the experimental spectrum (full line in Figure 3a). To support this thesis, we have performed, using the same approach, the simulation of the XANES spectra originated by the penta- and esa-coordinated Ti sites of the ETS-4 molecular sieve,[8] obtaining the dotted and dashed spectra reported in Figure 3b, respectively. It is worth noting that pentacoordinated site in ETS-4, of which the local symmetry should not differ strongly from that of terminal sites in ETS-10, results in a simulated XANES spectrum exhibiting an important pre-edge peak at almost the same energy as that of the peak observed in the experimental spectrum of ETS-10 (see vertical dotted line). The impressive increase undergone by the extinction coefficient of the pre-edge peaks in the XANES spectra, once a significant distortion of the $[TiO_6]$ units occurs (compare the dotted and

XAS Study of ETS-10 Titanosilicate

J. Phys. Chem. B, Vol. 109, No. 27, 2005 **13135**

dashed curves in Figure 3b), implies that the fraction of terminal Ti atoms responsible for the pre-edge peak at 4971.3 eV in ETS-10 should be a minority fraction of the overall Ti atoms. Unfortunately, a quantitative evaluation of this fraction is not straightforward, owing to the absence of a correct model of the defective Ti sites in ETS-10.

We can thus conclude that both the Wang–Damin and Sankar models fail in the precise reproduction of pre-edge features; however, we shall not enter into further detail for the discussion of the pre-edge features, because this is the spectral region where the simulations are less accurate, and the spectroscopic features of the experimental data are strongly affected by the presence of defects (e.g., Ti vacancies along the chains)[6,15] which cannot be simulated in a straightforward manner.

Regarding the discussion of the edge and post-edge features, both models are able to locate at the correct energy values the white line and the successive resonance (Figure 3a). The difference results in the relative intensity. The Wang–Damin model is able to better simulate the resonance intensities, while the Sankar model strongly underestimates the white line intensity (dotted line in Figure 3a). Furthermore, the Sankar model is unable to reproduce the complex feature in the 5000–5010 eV region. Conversely, this feature is present in the spectrum resulting from the Wang–Damin model (dashed line in Figure 3a). On the basis of the comparison between experimental and simulated XANES spectra, it emerges an overall better agreement with the Wang–Damin model.

3.2. EXAFS. The experimental EXAFS spectrum of ETS-10 is reported as a scattered line at the bottom of Figure 4. It is characterized by a high complexity. Several interference effects are clearly detected, and it is worth noting the strong beats around 8 and 10 Å^{-1} in k-space.

The GNXAS code works only in pure k-space and does not use the common Fourier filtering procedure.[28,29] This feature allows the code to simultaneously fit the experimental spectrum with a model and to search for the extraction of the EXAFS spectrum from the μx curve in the best agreement with the model. This procedure allows a reduction of the arbitrariness in the EXAFS extraction and the risk of excluding low-frequency components from the EXAFS spectra. Another important feature of the GNXAS software is the clever way of treating the different scattering paths that compose the theoretical signal. GNXAS uses signals that are the sum of more scattering paths that can be divided into two-, three-, and four-bodies signals. The last ones have not been used in this work. $\gamma^{(2)}$ signals are the sum of all the scattering paths that involve the absorber atom and a single scatterer, parametrized by (i) the coordination number, (ii) the Debye–Waller factor, and (iii) the distance. $\eta^{(3)}$ signals are the sum of all the scattering paths that involve the absorber atoms and two scattering atoms, parametrized by (i) the coordination number, (ii) the two distances for two shortest bonds involved in the triangle and (iii) their Debye–Waller factors, (iv) the value of the angle between the two previous bonds and (v) its Debye–Waller factor, and (vi) the correlation factor between the Debye–Waller factors of the bonds and of the angle.[37]

The cluster used to simulate the data has been reported in Figure 2. It represents the larger one adopted so far in the simulation of the EXAFS spectrum of ETS-10. The atoms for which scattering has been included in the simulations have been represented as full spheres, and the absorber is labeled Tia. Along the −Ti−O−Ti−O−Ti− chain, the cluster includes up to the second shell around Tia (O2 and Ti1 atoms: degeneration factor = 2), as it was for the cluster adopted by Sankar et al.[23]
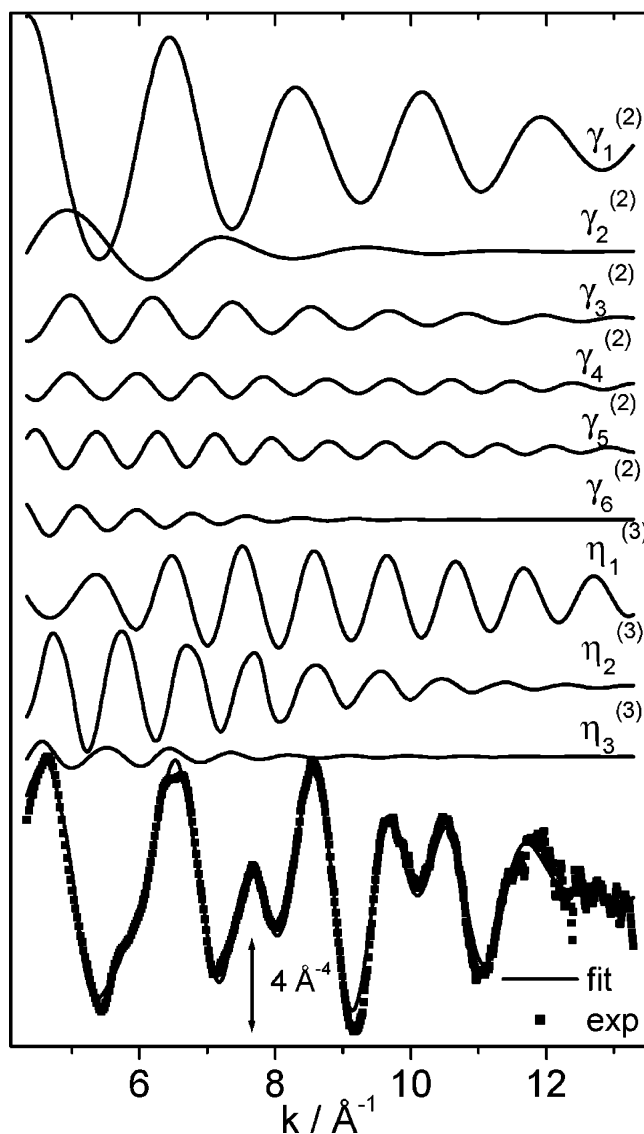
Figure 4. From top to bottom: (a) Different two ($\gamma_i^{(2)}$, $i = 1-6$)- and three ($\eta_j^{(3)}$, $j = 1-3$)]-body path contributions to the theoretical signal (for the definition of the single contributions, see text) and (b) superimposed experimental (scattered line) and best-fit spectra (full line).

In the direction perpendicular to the chain, in addition to the O1 and Si1 atoms (the only one included in the Sankar model and exhibiting a degeneration factor of 4), we have also taken into account O3, bridging two S1 atoms, and O4, bridging an S1 atom, and a further silicon atom not included in the simulation. Both O3 and O4 scatterers exhibit a degeneration factor of 4. Finally, extraframework sodium counterions, Na1, and the oxygen atoms coordinated to Ti1 perpendicularly to the chain, O5, have also been included in the simulation. They are four- and eightfold degenerated, respectively. In summary, the simulated EXAFS spectrum has been obtained as the sum of six $\gamma^{(2)}$ signals given by all the equivalent atoms (see the discussed degeneracy factors) to the ones labeled as O1 [$\gamma_1^{(2)}$], O2 [$\gamma_2^{(2)}$], Na1 [$\gamma_3^{(2)}$], O4 [$\gamma_4^{(2)}$], O5 [$\gamma_5^{(2)}$], O3 [$\gamma_6^{(2)}$], by two $\eta^{(3)}$ signals given by all the equivalent pairs of atoms (O1, Si1) [$\eta_1^{(3)}$] and (O2, Ti1) [$\eta_2^{(3)}$], and by an additional signal given by the collinear path (O1, O7), defined here as $\eta_3^{(3)}$;[38] see Figure 2 for the atom identification. According to the F test, the other possible signals, like the $\eta^{(3)}$ involving the two axial oxygen atoms (O2, O6) were statistically insignificant and have

TABLE 1: Summary of Distances and Angles in the ETS-10 Structure Optimized in the EXAFS Study Presented Here (last two columns)[a]

| structural variable	literature data			present work: EXAFS	
	ab initio periodic model (model II) [21]	XRD single crystal [16]	EXAFS [23]	mean value this work	σ^2 this work
Tia$-$O2	1.883 Å	1.872(1) Å	1.71 and 2.11 Å	1.87(1) Å	0.017(2) Å^2
Tia$-$O1	2.000 Å	1.99(1) Å	2.02 Å	2.05(1) Å	0.0050(5)Å^2
Tia$-$Na1	2.976 Å	3.15$-$3.20 Å	3.07 Å	3.05(2) Å	0.010(2) Å^2
Tia$-$O3	3.50 Å	3.74 Å		3.78(2) Å	0.006(1) Å^2
Tia$-$O4	4.05$-$4.15 Å	4.17 Å		4.10(3) Å	0.007(1) Å^2
Tia$-$O5	4.18$-$4.33 Å	4.23$-$4.25 Å		4.22(3) Å	0.023(3) Å^2
Tia$-$Ti1	3.759 Å	3.743 Å	3.76 Å	3.73 Å	0.014(2) Å^2
Tia$-$Si1	3.26$-$3.27 Å	3.27 Å	3.31 Å	3.32 Å	0.0053(6)Å^2
O1$-$Si1	1.61$-$1.62 Å	1.610 Å	1.63 Å	1.60(2) Å	0.0021(3)Å^2
Tia$-$O2$-$Ti1	172.6°	177.9°	165°	180(5)°	34(3) (°)^2
Tia$-$O1$-$Si1	128.6$-$129.8°	130.2°	130°	132(5)°	15(2) (°)^2

[a] For comparison, the analogous values available in the literature are reported for the ab initio work of Damin et al.[21] (second column), for the single-crystal XRD study of Wang and Jacobson[16] (third column), and for the previous EXAFS study of Sankar et al.[23] (fourth column). In the last work, oxygen atoms O3, O4, and O5 were not included in the model, and corresponding distances are consequently not available. Atom labeling refers to Figure 2.

consequently been omitted in the final fit because of their negligible amplitude.

The cluster has been built using the crystallographic information file (CIF) of Wang and Jacobson's refinement,[16] which basically agrees with the optimized structure obtained in Damin's[21] calculations. During the fit procedure, the O6 atom has been considered symmetrically equivalent to the O2 atom, while all remaining structural parameters were free to move. Of course, bond lengths and bond angles in $\eta^{(3)}$ signals must obey the geometrical constrains of a triangle. The quality of the fit obtained with the Wang$-$Damin model can be appreciated both in *k*-space (bottom curves in Figure 4) and in *R*-space (Figure 5).

At fit convergence, all the interatomic distances and angles reached values very close to those assigned by Wang and Jacobson[16] or by Damin et al.;[21] see Table 1. The dominating signals are the single scattering one generated by the four O1 atoms and the twofold degenerated multiple scattering one involving the O2 and Ti1 atoms along the chain, the $\gamma_1^{(2)}$, $\eta_1^{(3)}$, and $\eta_2^{(3)}$ signals in Figure 4, respectively. Conversely, the extremely high value of the Debye$-$Waller factor for the $\gamma_2^{(2)}$ signal (see Table 1) tends to minimize the contribution of the O2 atoms to the overall signal. This last feature mirrors the very high thermal parameter associated with O2 atoms resulting from the XRD refinement by Wang and Jacobson[16] and the vibration modes calculated by Damin et al.[21] that present, for O2, displacements from its relative equilibrium position much higher than for the other atoms of the cell. In particular, the analysis of the normal modes assigns the Raman 725 cm^{-1} fingerprint Raman mode of ETS-10 to a total symmetric combination of the Ti$-$O bond stretching involving only the oxygen atoms along the O$-$Ti$-$O$-$Ti$-$ wire[21] (i.e., O2 atoms actually). It is important to emphasize that, owing to both the weakness of the $\gamma_2^{(2)}$ contribution and its low *k*-frequency, its overall contribution to the EXAFS signal can be subjected to a severe underestimation if an accurate $\chi(k)$ extraction is not performed. This fact, which is particularly delicate for the ETS-10 case, emphasizes the importance of including the parameters of the $\chi(k)$ extraction within the fit of the structural parameters, as is done by the GNXAS approach.[28,37]

Subsequently, in addition, the symmetry constraints applied to the O2 and O6 atoms have been removed, and another fit procedure was launched in order to compare the Wang$-$Damin model with the Sankar one (we recall that this last model predicts two very different distances from the absorber for the
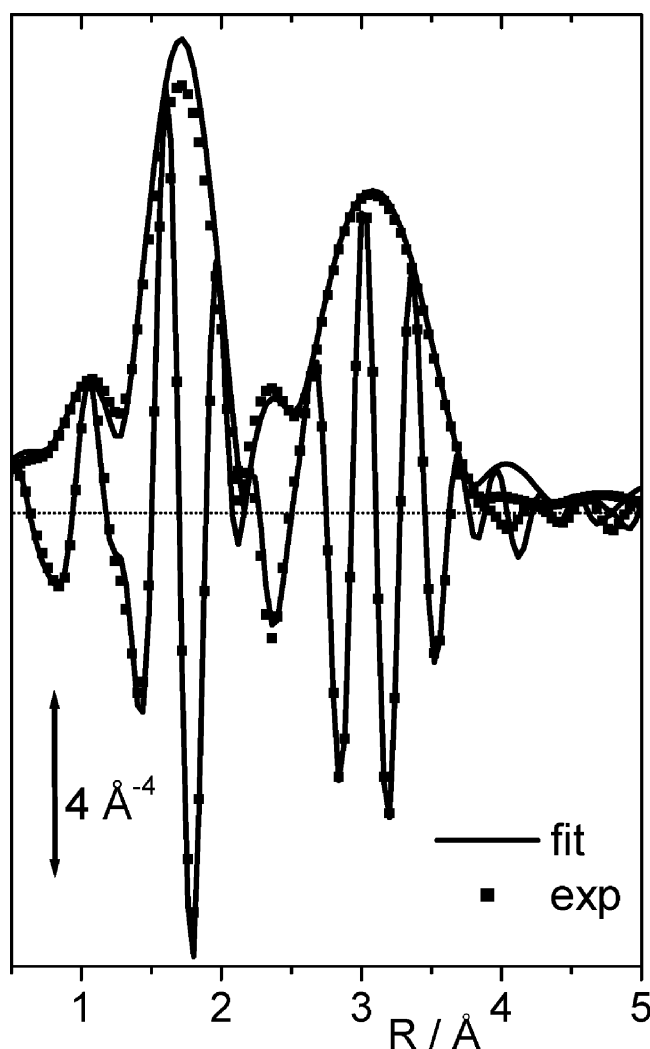
Figure 5. Fourier transform into *R* space of the k^3-weighted experimental (scattered line) and of its best fit (full line), that is, of the k^3 $\chi(k)$ functions reported at the bottom of Figure 4. Both the modulus and the imaginary part of the Fourier transforms are reported.

O2 and O6 atoms; see Figure 2). Although during this second fit the two distances were subjected to an unconstrained minimization (starting from Tia$-$O2 = 1.7 Å and Tia$-$O6 = 2.1 Å), the convergence point invariably resulted in a negligible difference between the two distances.

XAS Study of ETS-10 Titanosilicate

J. Phys. Chem. B, Vol. 109, No. 27, 2005 **13137**

4. Conclusion

Both EXAFS and XANES (edge and post-edge regions) spectroscopies support a model of ETS-10 where the Ti atoms are bonded with two equivalent axial oxygen atoms. On the basis of EXAFS results, the inability for XANES to reproduce the pre-edge region can also ascribed to the presence of defective Ti atoms at terminal positions of the Ti−O−Ti−O−Ti-chains. For the EXAFS data analysis, the GNXAS code has shown its power in the treatment of such a complex system, avoiding underestimation of the weak low k-component of the signal due to equatorial oxygen atoms during the extraction of the $\chi(k)$ function from the experimental absorption curve $\mu(E)x$.

Although both the EXAFS and XANES data reported here support the Wang−Damin model, the agreement between our results and the ab initio model[21] and experimental XRD data[16] is not total and is possibly subject to further discussion. To obtain an improvement in the knowledge of ETS-10, it will be mandatory to find the synthesis conditions in which it is favorable to grow only one of the two ideal polymorphs and/or where the Ti defectivity is strongly depressed, to allow a more straightforward interpretation of X-ray diffraction and absorption data, respectively.

References and Notes

(1) Taramasso, M.; Perego, G.; Notari, B. U.S. Patent 4,410,501, 1983.

(2) Notari, B. *Adv. Catal.* **1996**, *41*, 253−334.

(3) Bordiga, S.; Damin, A.; Bonino, F.; Ricchiardi, G.; Zecchina, A.; Tagliapietra, R.; Lamberti, C. *Phys. Chem. Chem. Phys.* **2003**, *5*, 4390−4393.

(4) Bonino, F.; Damin, A.; Ricchiardi, G.; Ricci, M.; Spanò, G.; D'Aloisio, R.; Zecchina, A.; Lamberti, C.; Prestipino, C.; Bordiga, S. *J. Phys. Chem. B* **2004**, *108*, 3573−3583.

(5) Ratnasamy, P.; Srinivas, D.; Knözinger, H. *Adv. Catal.* **2004**, *48*, 1−169.

(6) Kuznicki, M. U.S. Patent 4,853,202, 1989.

(7) Al-Attar, L.; Dyer, A.; Blackburn, R. *J. Radioanal. Nucl. Chem.* **2000**, *246*, 451−455.

(8) Rocha, J.; Anderson, M. W. *Eur. J. Inorg. Chem.* **2000**, 801−818.

(9) Blasco, T.; Camblor, M.; Corma, A.; Perez-Pariente, J. *J. Am. Chem. Soc.* **1993**, *115*, 11806−11813.

(10) Calza, P.; Paze, C.; Pelizzetti, E.; Zecchina, A. *Chem. Commun.* **2001**, 2130−2131.

(11) Howe, R. F.; Krisnandi, Y. K. *Chem. Commun.* **2001**, 1588−1589.

(12) Llabrés i Xamena, F. X.; Calza, P.; Lamberti, C.; Prestipino, C.; Damin, A.; Bordiga, S.; Pelizzetti, E.; Zecchina, A. *J. Am. Chem. Soc.* **2003**, *125*, 2264−2271.

(13) Anderson, M. W.; Terasaki, O.; Ohsuna, T.; Philippou, A.; Mackay, S. P.; Ferreira, A.; Rocha, J.; Lidin, S. *Nature (London)* **1994**, *367*, 347−351.

(14) Ohsuna, T.; Terasaki, O.; Watanabe, D.; Anderson, M. W.; Lidin, S. *Stud. Surf. Sci. Catal.* **1994**, *84*, 413−420.

(15) Anderson, M. W.; Terasaki, O.; Ohsuna, T.; Malley, P. J. O.; Philippou, A.; Mackay, S. P.; Ferreira, A.; Rocha, J.; Lidin, S. *Philos. Mag. B* **1995**, *71*, 813−841.

(16) Wang, X. Q.; Jacobson, A. J. *Chem. Commun.* **1999**, 973−974.

(17) Anderson, M. W.; Agger, J. R.; Hanif, N.; Terasaki, O. *Microporous Mesoporous Mater.* **2001**, *48*, 1−9.

(18) Borello, E.; Lamberti, C.; Bordiga, S.; Zecchina, A.; Otero Arean, C. *Appl. Phys. Lett.* **1997**, *71*, 2319−2321.

(19) Lamberti, C. *Microporous Mesoporous Mater.* **1999**, *30*, 155−163.

(20) Bordiga, S.; Palomino, G. T.; Zecchina, A.; Ranghino, G.; Giamello, E.; Lamberti, C. *J. Chem. Phys.* **2000**, *112*, 3859−3867.

(21) Damin, A.; Llabrés i Xamena, F. X.; Lamberti, C.; Civalleri, B.; Zicovich-Wilson, C. M.; Zecchina, A. *J. Phys. Chem. B* **2004**, *108*, 1328−1336.

(22) Davis, R. J.; Liu, Z.; Tabora, J. E.; Wieland, W. S. *Catal. Lett.* **1995**, *34*, 101−113.

(23) Sankar, G.; Bell, R. G.; Thomas, J. M.; Anderson, M. W.; Wright, P. A.; Rocha, J. *J. Phys. Chem.* **1996**, *100*, 449−452.

(24) Rainho, J. P.; Pillinger, M.; Carlos, L. D.; Ribeiro, S. J. L.; Almeida, R. M.; Rocha, J. *J. Mater. Chem.* **2002**, *12*, 1162−1168.

(25) Eldewik, A.; Howe, R. F. *Microporous Mesoporous Mater.* **2001**, *48*, 65−71.

(26) Southon, P. D.; Howe, R. F. *Chem. Mater.* **2002**, *14*, 4209−4218.

(27) Ankudinov, A. L.; Ravel, B.; Rehr, J. J.; Conradson, S. D. *Phys. Rev. B* **1998**, *58*, 7565−7576.

(28) Filipponi, A.; DiCicco, A.; Natoli, C. R. *Phys. Rev. B* **1995**, *52*, 15122−15134.

(29) Filipponi, A.; DiCicco, A. *Phys. Rev. B* **1995**, *52*, 15135−15149.

(30) Zecchina, A.; Otero Arean, C.; Turnes Palomino, G.; Geobaldo, F.; Lamberti, C.; Spoto, G.; Bordiga, S. *Phys. Chem. Chem. Phys.* **1999**, *1*, 1649−1657.

(31) Lamberti, C.; Bordiga, S.; Bonino, F.; Prestipino, C.; Berlier, G.; Capello, L.; D'Acapito, F.; Xamena, F.; Zecchina, A. *Phys. Chem. Chem. Phys.* **2003**, *5*, 4502−4509.

(32) Lamberti, C.; Prestipino, C.; Bordiga, S.; Berlier, G.; Spoto, G.; Zecchina, A.; Laloni, A.; La Manna, F.; D'Anca, F.; Felici, R.; D'Acapito, F.; Roy, P. *Nucl. Instrum. Methods Phys. Res., Sect. B* **2003**, *200*, 196−201.

(33) Cabaret, D.; Joly, Y.; Renevier, H.; Natoli, C. R. *J. Synchrotron Radiat.* **1999**, *6*, 258−260.

(34) Wu, Z. Y.; Ouvrard, G.; Gressier, P.; Natoli, C. R. *Phys. Rev. B* **1997**, *55*, 10382−10391.

(35) Bordiga, S.; Coluccia, S.; Lamberti, C.; Marchese, L.; Zecchina, A.; Boscherini, F.; Buffa, F.; Genoni, F.; Leofanti, G.; Petrini, G.; Vlaic, G. *J. Phys. Chem.* **1994**, *98*, 4125−4132.

(36) Ricchiardi, G.; Damin, A.; Bordiga, S.; Lamberti, C.; Spanò, G.; Rivetti, F.; Zecchina, A. *J. Am. Chem. Soc.* **2001**, *123*, 11409−11419.

(37) Filipponi, A.; DiCicco, A. *Task Quarterly* **2000**, *4*, 575−669.

(38) Note that in the GNXAS nomenclature these kind of paths are labeled as $\gamma^{(3)}$. For the sake of brevity, we will not enter into a full illustration of the code nomenclature here.